

A Blessing and a Curse: How a Supercapacitor's Large Capacitance Causes its Slow Charging

Cheng Lian,^{1,*} Mathijs Janssen,^{1,2,3} Honglai Liu,⁴ and René van Roij¹

¹*Institute for Theoretical Physics, Center for Extreme Matter and Emergent Phenomena, Utrecht University, Princetonplein 5, 3584 CC Utrecht, The Netherlands*

²*Max-Planck-Institut für Intelligente Systeme, Heisenbergstraße 3, 70569 Stuttgart, Germany*

³*Institut für Theoretische Physik IV, Universität Stuttgart, Pfaffenwaldring 57, 70569 Stuttgart, Germany*

⁴*State Key Laboratory of Chemical Engineering, School of Chemistry and Molecular Engineering, East China University of Science and Technology, Shanghai 200237, China*

(Dated: November 15, 2021)

The development of novel electrolytes and electrodes for supercapacitors is hindered by a gap of several orders of magnitude between experimentally measured and theoretically predicted charging timescales. Here, we propose an electrode model, containing many parallel stacked electrodes, that explains the slow charging dynamics of supercapacitors. At low applied potentials, the charging behavior of this model is described well by an equivalent circuit model. Conversely, at high potentials, charging dynamics slow down and evolve on two relaxation time scales: a generalized RC time and a diffusion time, which, interestingly, become similar for porous electrodes. The charging behavior of the stack-electrode model presented here helps to understand the charging dynamics of porous electrodes and qualitatively agrees with experimental time scales measured with porous electrodes.

In the electric energy storage domain, supercapacitors [Fig. 1(a)] have proven their value in applications requiring higher power output than delivered by batteries and more energy than stored in dielectric capacitors [1–4]. Many types of carbon-based materials have been used for the capacitor's electrodes [5–7]. However, the relation between the porous structures and the charging dynamics of macroscopic supercapacitors is poorly understood. On the one hand, transmission line (TL) models [8–11] can successfully fit experimental data, but the fit parameters therein do not have a direct interpretation in terms of microscopic properties of supercapacitors. On the other hand, molecular dynamics simulation [12–18], lattice Boltzmann simulations [19, 20], and classical dynamic density functional theory [21–23] can elucidate the charging mechanisms of a single or a few nanopores or a nanoscale anode-cathode model, but predicted relaxation time scales are of the order of ns, roughly 12 orders of magnitude smaller than experimentally measured 10^3 s timescales of supercapacitors [24–27]. These long charging times, however, can be decently approximated by multiplying a nanocapacitor's RC time by the squared ratio of nanocapacitor-to-supercapacitor thicknesses [14, 18]. Even though such approaches to bridge scales are valuable, they ignore the actual multiscale character of the system, e.g. the transport of ions through quasi-neutral macropores. To faithfully describe the charging of supercapacitors, one should account for both the ionic currents from the ion reservoir that separates anode and cathode through a macropore network into the nanopores (micrometers) and for the electric double layer (EDL) buildup therein (nanometers). Clearly, such a multiscale analysis cannot be performed

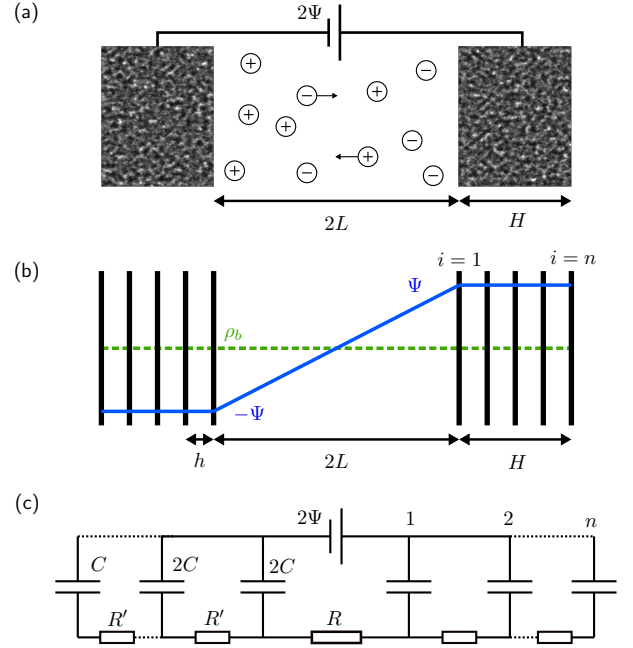


Figure 1. (a) Sketch of a supercapacitor containing a 1:1 electrolyte, two porous electrodes, and a battery providing an electrostatic potential difference 2Ψ . (b) In our stack-electrode model, the cathode and anode each contain n planar electrodes at intervals of h . Initial anionic and cationic densities are ρ_b throughout the cell. At time $t = 0$, $-\Psi$ and $+\Psi$ are applied to all electrodes on the left and right-hand sides of the system, respectively. (c) Equivalent circuit model for the stack-electrode model.

with the above mentioned simulation techniques alone, as computational power limits simulations to nanoscale systems. In this article, we present a minimal model to explain the long experimental relaxation timescales of supercapacitors instead.

* c.lian@uu.nl

The canonical model describing ionic charge relaxation to an applied electric field employs a dilute 1:1 electrolyte and two parallel and planar blocking electrodes separated by a distance $2L$ [28]. Suddenly applying a potential difference 2Ψ with a battery, the two electrodes will acquire opposite surface charge densities $\pm e\sigma(t)$, eventually screened in the electrolyte by two EDLs, whose equilibrium width is characterized by the Debye length $\kappa^{-1} = \sqrt{\varepsilon k_B T / 2e^2 \rho_b}$, with $2\rho_b$ the bulk ion number density, ε the electrolyte permittivity, e the elementary charge, and $k_B T$ the thermal energy. At late times and for $\kappa L \gg 1$, $\sigma(t) = 2\Phi \rho_b \kappa^{-1} [1 - \exp(-t/\tau_{RC})]$, with $2\Phi = 2e\Psi/k_B T$ the dimensionless applied potential, $\tau_{RC} = \kappa^{-1} L/D$ the RC time, and D the ionic diffusion coefficient [28–30]. Inserting typical experimental parameters $\kappa^{-1} \approx 1$ nm, $L \approx 250$ μ m, and $D \approx 1 \times 10^{-9}$ m² s⁻¹ yields $\tau_{RC} \approx 10^{-4}$ s: larger than the timescales predicted by molecular simulations, but still 5 orders of magnitude smaller than the experimental charging time of supercapacitors. This discrepancy comes as no surprise as the above $\sigma(t)$ applies to planar electrodes: this model does not account for the huge surface area and for the ion transport through the porous structure of the supercapacitor electrodes. Simple extensions of the flat electrode setup were discussed, such as spherical and cylindrical electrodes [20, 31] and a single cylindrical pore in contact with a reservoir [9]. Several theoretical works focused on the charging dynamics of porous electrodes [32–38]. Still, the gap between experimental and theoretical supercapacitor charging timescales has not been bridged yet.

To explain why the charging time of macroscopic porous electrodes [Fig. 1(a)] is much larger than that of flat electrodes, in this article, we will characterize the charging dynamics of the model shown in Fig. 1(b) and also compare it to the charging dynamics of the circuit shown in Fig. 1(c). In our model, the nanoporous cathode and anode of a supercapacitor are both modeled by a stack of n parallel electrodes with an equal spacing h mimicking the pore size, such that the thickness of the cathode and anode equals $H = (n-1)h$. The surface area A of all individual electrodes is assumed to be sufficiently large that we can ignore edge effects and study all microscopic observables as a function of a single coordinate x perpendicular to the electrode surfaces. We adopt a coordinate system whose origin lies in the middle ($x = 0$) of the system and where the i th cathode and anode, with $i = \{1, \dots, n\}$, are located at $X_i = \pm[L + (i-1)h]$. All parallel stacked electrodes are fully permeable to the electrolyte in order to mimic the porosity of supercapacitor electrodes, except the two outer ones ($i = n$) which are impermeable to have a closed system [cf. Eq. (2b)]. Thus, the ionic number densities $\rho_{\pm}(x, t)$ and ionic fluxes $j_{\pm}(x, t)$ are continuous at each X_i . Initially, the ionic number densities are homogenous

$$\rho_{\pm}(x, t = 0) = \rho_b, \quad |x| \leq L + H. \quad (1)$$

At time $t = 0$, a dimensionless potential difference 2Φ

is applied to the macroscopic cathode and anode. This yields the following boundary conditions for $t > 0$,

$$\phi(\pm X_i, t) = \pm \Phi; \quad (2a)$$

$$j_{\pm}(\pm X_n, t) = 0, \quad (2b)$$

with $\phi(x, t)$ the electric potential in units of the thermal voltage $k_B T/e$. To model the ionic dynamics, we use the classical Poisson-Nernst-Planck (PNP) equations [28]

$$\partial_x^2 \phi(x, t) = -\kappa^2 \left[\frac{\rho_+(x, t) - \rho_-(x, t)}{2\rho_b} \right]; \quad (3a)$$

$$\partial_t \rho_{\pm}(x, t) = -\partial_x j_{\pm}(x, t); \quad (3b)$$

$$j_{\pm}(x, t) = -D [\partial_x \rho_{\pm}(x, t) \pm \rho_{\pm}(x, t) \partial_x \phi(x, t)]. \quad (3c)$$

In Eqs. (1)–(3) appear the applied potential Φ and four length scales: h , H , L , and κ^{-1} . With these parameters, we can construct many different combinations that yield 1+3 independent dimensionless parameters, for instance: Φ , κL , κH , and κh or, equivalently, Φ , κL , H/L , and n . Here, we focus on the latter choice and mostly restrict to $H/L = 1$, which is reasonable for supercapacitors.

In Fig. 2(a), we present numerical results for $\phi(x, t)$ for a low potential $\Phi = 0.001$ and $\kappa L = 100$, $H/L = 1$, and $n = 5$. These parameters correspond to $\kappa h = 25$, which means that the EDLs are thin compared to the electrode separations. Initially, the potential in the reservoir ($|x| < L$) displays a typical linear x dependence, which corresponds to a spatially constant electric field. At later times, the potential retains this linear dependence in the reservoir, albeit with a slope that decreases with time due to the buildup of EDLs. At short times $t/\tau_{RC} \leq 20$, there is a clear asymmetry between the two EDLs that surround individual planar electrodes. This asymmetry is lost at later times $t \geq 20\tau_{RC}$, when the EDLs fully equilibrate.

For the same parameters, in Fig. 2(b) we show the surface charge densities $e\sigma_i$ of the individual electrodes (labeled with i), which we find with Gauss' law $\sigma_i(t) = -2\rho_b \kappa^{-2} [\partial_x \phi|_{X_i^+} - \partial_x \phi|_{X_i^-}]$. At early times $t < \tau_{RC}$, the electrodes charge faster the closer they are situated to

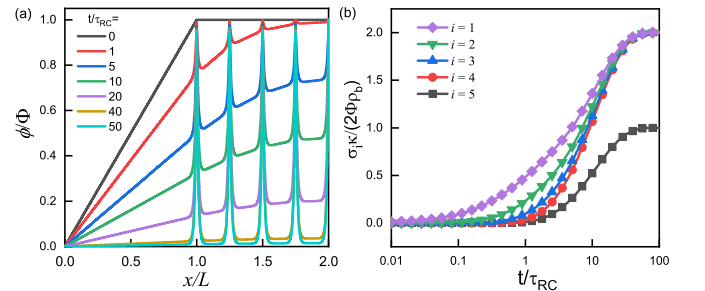


Figure 2. Time dependence of the scaled (a) potential $\phi(x, t)$ and (b) the surface charge densities $\sigma_i(t)$ for $i = \{1, \dots, 5\}$ of the electrode for $\Phi = 0.001$, $\kappa L = 100$, $H/L = 1$, and $n = 5$. The symbols and lines in (b) correspond to numerical and equivalent-circuit model calculations, respectively.

the reservoir, $\sigma_1 > \sigma_2 > \dots > \sigma_n$. However, the late-time relaxation timescale is the same for all electrodes: all electrodes reach 99.9% of their equilibrium charge around $t/\tau_{RC} \approx 50$. As the outer electrodes face the electrolyte only at one side, we have $\partial_x \phi|_{X_n^+} = \partial_x \phi|_{-X_n^-} = 0$, and $\sigma_n(t/\tau_{RC} \rightarrow \infty)$ is a factor of two smaller than the other electrodes. To better understand these phenomena, we studied the behavior of the circuit model shown in Fig. 1(c). Note the great similarity of this model to traditional TL models used for fitting experimental data: the only difference is the capacitance C of the outermost capacitor, rather than $2C$ in the TL model (see also Appendix A4). However, in contrast to the TL model, where R , C , and n are fit parameters, the elements of the circuit in Fig. 1(c) are all one-to-one related to electrolyte and electrode properties of our microscopic model, $R = 2L/(A\epsilon\kappa^2D)$ and $C = A\epsilon\kappa$. In Appendix A we derive a matrix differential equation [cf. Eq. A12] that relates the potential drops over the n capacitors to the currents through the n resistors. With the solution to this equation, we find predictions for the time-dependent charge on each capacitor in this circuit, which translates into a prediction for $\sigma_i(t)$ in the corresponding microscopic model, shown in Fig. 2(b) with symbols. Clearly, the predictions from the microscopic and circuit model are indistinguishable. In line with our earlier observation, the equivalent-circuit model predicts that all electrodes relax exponentially at late times with the same time constant τ_n

$$\frac{\tau_n}{\tau_{RC}} = \left(2 + 0.75 \frac{H}{L}\right) n - 1 - 0.91 \frac{H}{L}, \quad (4)$$

which correctly reduces to $\tau_1 = \tau_{RC}$ for $n = 1$ (for which $H/L = 0$). The coefficients 2 and 1 appearing in Eq. (4) are analytical results obtained in the limit $H/L \rightarrow 0$; the other numerical factors relate to the smallest eigenvalue of the almost-Toeplitz matrix in the afore-mentioned matrix differential equation A12. From Eq. (4) we see that τ_n is large whenever n is large. This suggests that the large relaxation time of supercapacitors stems from their large internal surface area, achieved through many small pores. Interestingly, Eq. (4) recovers the electronic circuit intuition that a supercapacitor should charge slower the larger its electrode surface area. This areal scaling is not present in the relaxation time τ_{RC} of Ref. [28] as, in that work, R and C scale oppositely with A .

Because supercapacitors are typically subjected to large potentials in practical applications, we also characterize the dynamics of the stack-electrode model at $\Phi > 1$. In Figs. 3(a), 3(c), and 3(e) we present data for $\Phi = \{0.01, 0.1, 1, 2\}$, $\kappa L = 100$, and $n = 1$ (hence, $H/L = 0$). For this two-electrode setup, it is known that, next to τ_{RC} , the diffusion time L^2/D emerges in the ionic relaxation due to slow salt diffusion from the cell center to the electrode surfaces [28, 30, 39]. Indeed, Fig. 3(a) shows that the normalized surface density $\sigma_n(t)/\sigma_{eq}$, with $\sigma_{eq} \equiv \sigma_n(t/\tau_{RC} \rightarrow \infty)$ the late-time surface charge density, develops slower at higher

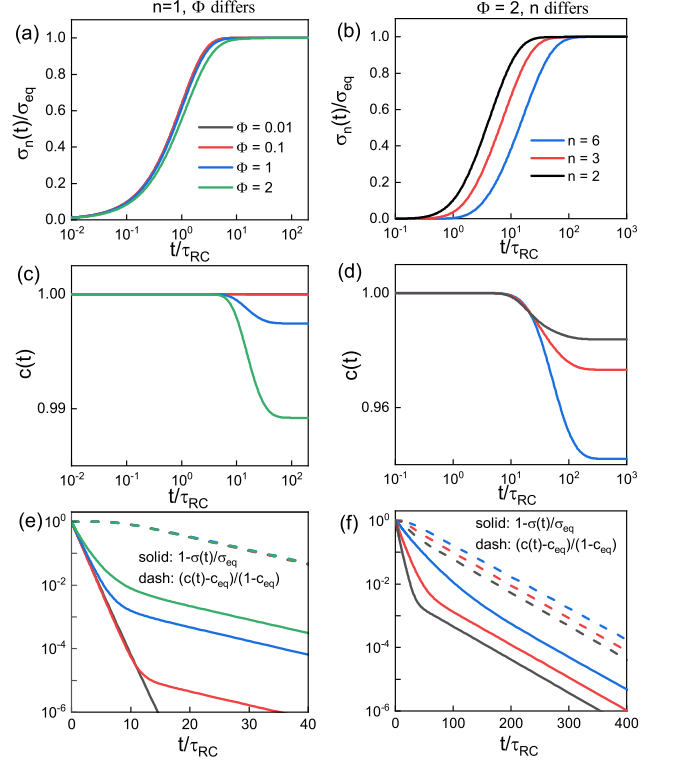


Figure 3. The surface charge density (a), (b) $\sigma(t)/\sigma_{eq}$, the salt concentration at the cell center (c), (d) $c(t)$, and the charge relaxation (e), (f) $1 - \sigma(t)/\sigma_{eq}$ (solid lines) and the concentration decay $[c(t) - c_{eq}]/[c(0) - c_{eq}]$ (dashed lines) of the stack-electrode model for $\kappa L = 100$, in (a), (c), and (e) for $n = 1$, $H/L = 0$ at potentials $\Phi = \{0.01, 0.1, 1, 2\}$, and in (b), (d), and (f) for $\Phi = 2$ and $H/L = 1$, at $n = \{2, 3, 6\}$.

Φ . Next, Fig. 3(c) shows the salt concentration at the cell center $c(t) = [\rho_+(0, t) + \rho_-(0, t)]/(2\rho_b)$ for the same Φ . We see that $c(t) \approx 1$ for $\Phi \leq 0.1$ and that $c(t)$ decreases at late times ($t/\tau_{RC} > 10$) by 0.25% and 1% for $\Phi = 1$ and 2: As our setup is closed, a net ionic adsorption on the electrodes “desalinates” the cell center [40]. To investigate the emergence of the slow timescale at large applied potentials, in Fig 3(e), we show the charge relaxation $1 - \sigma(t)/\sigma_{eq}$ (solid lines) and the concentration decay $[c(t) - c_{eq}]/[1 - c_{eq}]$ (dashed lines), where $c_{eq} \equiv c(t/\tau_{RC} \rightarrow \infty)$. At early times ($t/\tau_{RC} < 1$), all data for $1 - \sigma(t)/\sigma_{eq}$ collapse onto the $\Phi = 0.01$ curve, indicating that the initial ionic relaxation is described well by the equivalent circuit model, even for higher Φ . Thereafter, a second, slower relaxation emerges in $1 - \sigma(t)/\sigma_{eq}$, emerging more dominantly for higher Φ . At late times, the slopes of $1 - \sigma(t)/\sigma_{eq}$ and $[c(t) - c_{eq}]/[1 - c_{eq}]$ are the same. Numerical results [cf. Fig. B2(d)] for the adsorption timescale τ_{ad} , the inverse of these slopes, show that τ_{ad}/τ_{RC} is independent of Φ (for all Φ considered) and scales linearly with κL . Using the definition of τ_{RC} , we then recover the L^2/D scaling of τ_{ad} suggested by Ref. [28, 30]. In Appendix C, we check the robustness

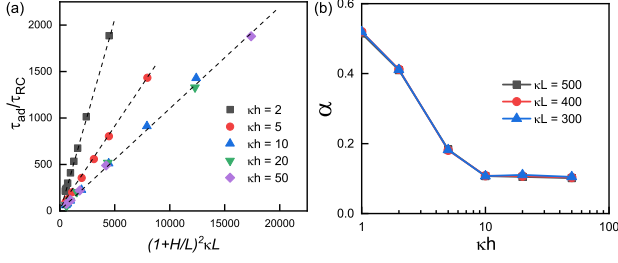


Figure 4. (a) The dependence of the (scaled) adsorption timescale τ_{ad} on the (scaled) system size $(L + H)^2$ for $\kappa L = 500$ at potential $\Phi = 2$ at several pore sizes $\kappa h = \{2, 5, 10, 20, 50\}$ and $n = \{2, 5, 10, 20, 50, 100, 150, 200, 300\}$, with $n = 200$ and $n = 300$ for $\kappa h = 20$ and $\kappa h = 50$ off the scale of the plot. (b) The prefactor α of [Eq. (5)] as a function of κh for $\kappa L = 500$ with a linear fit through the data in (a); $\kappa L = 300$ and 400 with identical results.

of our findings with dynamical density functional theory calculations of a room temperature ionic liquid at the experimentally realistic voltage $\Psi = 0.5$ V: Figure C1 shows that the surface charge again relaxes with two distinct relaxation times.

To investigate the effect of $n > 1$ for high potentials, in Figs. 3(b), 3(d), and 3(f), we plot the same observables as in Figs. 3(a), 3(c), and 3(e), now for $\Phi = 2$, $\kappa L = 100$, $H/L = 1$, and $n = \{2, 3, 6\}$. Similar to our $\Phi = 0.001$ findings [condensed in τ_n of Eq. (4)], we see that the charging dynamics at $\Phi = 2$ also slows down with increasing n . The salt concentration at the cell center $c(t)$ [Fig. 3(d)] is again unaffected at early times $t/\tau_{RC} < 5$, after which it decays to an equilibrium value that decreases with n . Thus, our model recovers the intuition that, for two electrodes of the same volume, the one with more pores (and, hence, a large surface area) desalinates an electrolyte reservoir more. In Fig. 3(f), we see that the surface charge again decays on two distinct timescales. Plotting the same data with time scaled by τ_n instead of by τ_{RC} [cf. Fig. B3(c)], all $1 - \sigma(t)/\sigma_{eq}$ collapse for $t \leq \tau_n$, which shows that the circuit model decently describes the early-time relaxation at high potentials as well. Conversely, at late times, we see in Fig. 3(f) that $1 - \sigma(t)/\sigma_{eq}$ and $[c(t) - c_{eq}]/[1 - c_{eq}]$ decay exponentially with a time constant τ_{ad} that does not depend on n for the parameter set under consideration. Considering a larger set of κL , κh , and n , we show τ_{ad} in Fig. 4(a). From this figure we conclude that

$$\tau_{\text{ad}} = \alpha \frac{(H + L)^2}{D}, \quad (5)$$

hence, the adsorption time τ_{ad} depends on the total system size. We show the κh -dependent prefactor α in Fig. 4(b) for various κL , which reveals that α is κL independent and that $\alpha \approx 0.1$ for $\kappa h > 10$, while α increases with decreasing $\kappa h \leq 10$.

Since τ_n [Eq. (4)] and τ_{ad} [Eq. (5)] depend on κL , κh , and n differently, both $\tau_{\text{ad}}/\tau_n \ll 1$, $\tau_{\text{ad}}/\tau_n \approx 1$, and

$\tau_{\text{ad}}/\tau_n \gg 1$ are possible. Focusing here on $n \gg 1$, which is relevant to macroscopic electrodes, we find

$$\frac{\tau_n}{\tau_{\text{ad}}} \approx \begin{cases} \frac{0.75}{\alpha \kappa h} \frac{H}{L} & L \gg H; \\ \frac{0.69}{\alpha \kappa h} & L = H; \\ \frac{2}{\alpha \kappa h} \frac{H}{L} & L \ll H. \end{cases} \quad (6)$$

For $H/L = 1$ (and $n \gg 1$) we find that $\tau_n/\tau_{\text{ad}} \sim 1$ whenever $\kappa h < 10$.

Finally, it is interesting to determine the applicability of our stack-electrode model to experiments: Here, we consider the setup of Ref. [26], where two carbon electrodes of thickness $H = 0.5$ mm, separation $2L = 2.2$ mm, porosity $p = 0.65$, mass density $\rho = 5.8 \times 10^5$ g m $^{-3}$, and Brunauer-Emmett-Teller-area $A_{\text{BET}} = 1330$ m 2 g $^{-1}$ were used. Assuming each porous electrode to consist of two flat solid carbon slabs, we get a crude estimate for the pore size with $h = p/(\rho A_{\text{BET}}) = 0.84$ nm. The electrodes were immersed in a 1 M NaCl solution at room temperature, hence, $\kappa^{-1} = 0.3$ nm and bulk diffusivity $D = 1.6 \times 10^{-9}$ m 2 s $^{-1}$. [We ignore that D is smaller in nanopores [32, 41] and that different diffusivities may appear in Eqs. (4) and (5) [42].] These parameters correspond, in our model, to $H/L = 0.45$, $n = 5.9 \times 10^5$, and $\kappa h = 2.8$, hence, $\alpha = 0.3$. With Eqs. (4) and (5) we now find $\tau_n = 2.9 \times 10^2$ s and $\tau_{\text{ad}} = 4.8 \times 10^2$ s, roughly within 1 order of magnitude from the two timescales (2×10^2 s and 9×10^3 s) observed in the experimental data of Ref. [26] (see Appendix D). Given the simplicity of our model and crudeness of our estimates of κh , n , and D , the remaining discrepancies are not surprising. Yet, the stack-electrode model has bridged the 5-orders-of-magnitude gap between experimental relaxation times and those predicted in the $n = 1$ model.

In summary, we studied the charging dynamics of nanoporous electrodes with a simple electrode model. At small applied potentials, numerical simulations of the PNP equations are reproduced accurately by an equivalent circuit model. This circuit model is akin to TL models used often to fit experimental supercapacitor data. Notably, however, the resistances, capacitances, and number of branches in the circuit model are not fit parameters but physically determined by our microscopic model. This one-to-one relation allows us to interpret the long relaxation time of supercapacitors as being due to the large number n of pores in nanoporous electrodes: The stack-electrode model relaxes with the timescale $\tau_n \sim (2 + 0.75H/L)n\tau_{RC}$. At higher potentials, the surface charge still relaxes at early times with τ_n . Higher potentials also lead to slow salt adsorption in the EDLs and concomitant depletion of the reservoir on the timescale $\tau_{\text{ad}} \sim (L + H)^2/D$. As salt and charge transport are coupled, the long timescale τ_{ad} also governs the late-time surface charge relaxation, all the more so the higher the applied potential. The two timescales τ_n

and τ_{ad} differ orders of magnitude for small n but become similar when electrodes have many pores, as is the case for supercapacitors. Inserting parameters relating to a recent experimental study [26], our simple model predicts the two observed relaxation times roughly within 1 order of magnitude. Our model thus successfully bridged the 5-orders-of-magnitude gap between theoretically predicted and experimentally measured timescales, and could serve as a basis for extensions that break the planar symmetry. However, more work is needed to fully understand the charging dynamics of porous electrodes, which should include effects due to finite ion sizes, more realistic modeling of pore morphology, Faradaic reactions, position-dependent diffusion coefficients, etc.

ACKNOWLEDGMENTS

C.L. and M.J. contributed equally to this work. This work is part of the D-ITP consortium, a program of the Netherlands Organisation for Scientific Research (NWO) that is funded by the Dutch Ministry of Education, Culture and Science (OCW). C.L. and R. v. R. acknowledge the EU-FET project NANOPHLOW (REP-766972-1), M.J. acknowledges support from S. Dietrich, and H.L. acknowledges NSFC (Grants. No. 91834301 and No. 21808055). We kindly thank Pieter Kouzyer for helpful discussions, Ben Ern   for access to the experimental data of Ref. [26], and Sviatoslav Kondrat for comments on our manuscript.

Appendix A: Equivalent circuit model

We discuss an equivalent circuit model that describes the charging dynamics of the stack-electrode model well (see also Ref. [43]). Before turning to the general n case, we first discuss the easier $n = 1$ and $n = 2$ cases.

1. The case $n = 1$

The trivial $n = 1$ case can be described by the circuit model shown in Fig. A1. The EDLs on each electrode are modeled with a capacitor of capacitance C . The electrolyte resistance is modeled through a resistor of resistance R . At $t = 0$ a voltage source is switched on

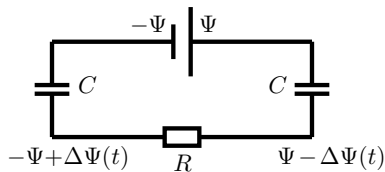


Figure A1. Equivalent circuit model for the stack electrode model in the trivial case $n = 1$.

to provide a potential difference of 2Ψ . The capacitors, initially uncharged, will acquire a charge $Q(t) = C\Delta\Psi(t)$ with $\Delta\Psi(t)$ being the time-dependent voltage difference between either sides of the capacitors. The current that flows through the system is found via Ohm's law, $IR = [\Psi - \Delta\Psi(t)] - [-\Psi + \Delta\Psi(t)] = 2[\Psi - \Delta\Psi(t)]$. With $I = \dot{Q}(t) = C\Delta\dot{\Psi}(t)$, we find

$$\Delta\dot{\Psi}(t) = [\Psi - \Delta\Psi(t)] \frac{2}{RC}, \quad (\text{A1a})$$

$$\Delta\Psi(t = 0) = 0, \quad (\text{A1b})$$

which is solved by

$$\Delta\Psi(t) = \Psi \left[1 - \exp\left(-\frac{2t}{RC}\right) \right]. \quad (\text{A2})$$

To relate this result to the relaxation of EDLs that we are trying to mimic, note that the EDL capacitance and electrolyte resistivity read $C = A\epsilon\kappa$ and $R = 2L/(A\epsilon\kappa^2D)$, respectively; hence, $RC = 2\tau_{RC} = 2\kappa^{-1}L/D$.

2. The case $n = 2$

For $n = 2$, we need to account for the fact that the inner electrode ($i = 1$) is facing the electrolyte twice, while the outer electrode ($i = 2$) faces it only once: we use $2C$ and C for the different capacitors, respectively, see Fig. A2. For this circuit, the charge on each of the capac-

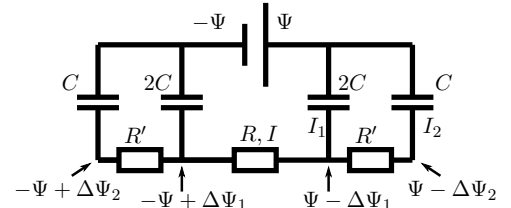


Figure A2. Equivalent circuit model for the stack electrode model at $n = 2$.

itors (index increasing outwards) is $Q_1(t) = 2C\Delta\Psi_1(t)$ and $Q_2(t) = C\Delta\Psi_2(t)$. Meanwhile, for the currents I , I_1 , and I_2 we have $I = I_1 + I_2$ (Kirchhoff's law), and $IR = 2[\Psi - \Delta\Psi_1(t)]$ and $I_2R' = \Delta\Psi_1(t) - \Delta\Psi_2(t)$ (Ohm's law). Combining the above equations gives two coupled differential equations

$$\Delta\dot{\Psi}_1(t) = \frac{I_1}{2C} = \frac{\Psi}{RC} - \left(\frac{1}{RC} + \frac{1}{2R'C} \right) \Delta\Psi_1(t) + \frac{1}{2R'C} \Delta\Psi_2(t), \quad (\text{A3a})$$

$$\Delta\dot{\Psi}_2(t) = \frac{I_2}{C} = \frac{1}{R'C} \Delta\Psi_1(t) - \frac{1}{R'C} \Delta\Psi_2(t), \quad (\text{A3b})$$

subject to the initial conditions

$$\Delta\Psi_1(t = 0) = 0, \quad (\text{A4a})$$

$$\Delta\Psi_2(t = 0) = 0. \quad (\text{A4b})$$

In matrix form, Eq. (A3) reads

$$\begin{pmatrix} \dot{\Delta\Psi_1(t)} \\ \dot{\Delta\Psi_2(t)} \end{pmatrix} = -\frac{1}{2R'C} \begin{pmatrix} 1+2R'/R & -1 \\ -2 & 2 \end{pmatrix} \begin{pmatrix} \Delta\Psi_1(t) \\ \Delta\Psi_2(t) \end{pmatrix} + \frac{\Psi}{RC} \begin{pmatrix} 1 \\ 0 \end{pmatrix}, \quad (\text{A5})$$

which can be written as $\dot{X} = Y - MX$, with

$$\begin{aligned} X &\equiv \begin{pmatrix} \Delta\Psi_1(t) \\ \Delta\Psi_2(t) \end{pmatrix}, \quad Y \equiv \frac{\Psi}{RC} \begin{pmatrix} 1 \\ 0 \end{pmatrix}, \\ M &\equiv \frac{1}{2R'C} \begin{pmatrix} 1+2R'/R & -1 \\ -2 & 2 \end{pmatrix} \equiv UDU^{-1}, \quad (\text{A6}) \end{aligned}$$

with $UU^{-1} = U^{-1}U = 1$ and $D = \frac{1}{2R'C} \begin{pmatrix} \lambda_+ & 0 \\ 0 & \lambda_- \end{pmatrix}$. Here, U is composed of the orthonormal eigenvectors of M , with eigenvalues λ_{\pm} . To find the formal solution to $\dot{X} = Y - MX$, note that $U^{-1}\dot{X}(t) = U^{-1}Y - DU^{-1}X(t)$ is solved by $U^{-1}X(t) = \exp[-Dt]a + D^{-1}U^{-1}Y$. The constant a is fixed by the boundary condition $U^{-1}X(t=0) = 0$,

$$\begin{aligned} U^{-1}X(0) &= a + D^{-1}U^{-1}Y = 0 \\ \Rightarrow a &= -D^{-1}U^{-1}Y, \end{aligned} \quad (\text{A7})$$

such that the full solution reads $X(t) = U(1 - \exp[-Dt])D^{-1}U^{-1}Y$, which can be written as

$$X(t) = U \begin{pmatrix} \left[1 - \exp\left(-\frac{\lambda_+ t}{2R'C}\right)\right] \frac{1}{\lambda_+} \\ 0 \\ \left[1 - \exp\left(-\frac{\lambda_- t}{2R'C}\right)\right] \frac{1}{\lambda_-} \end{pmatrix} U^{-1}Y.$$

We see that the late-time relaxation of $X(t)$ is determined by the smallest eigenvalue of M . For the stack electrode system, the resistance scales linearly with the width of the respective electrolyte regions. Specifying to $H = L$, we find $R'/R = H/(2L) = 1/2$. The eigenvalues of M then follow from $(2 - \lambda)(2 - \lambda) - 2 = 0$, which amounts to $\lambda_{\pm} = 2 \pm \sqrt{2}$. We see that the long-time relaxation is determined by $\tau = 2R'C/\lambda_- = RC/\lambda_- = (2 + \sqrt{2})\kappa^{-1}L/D$.

3. General n case

We redraw Fig. 1(c) and introduce additional notation in Fig. A3. Similar to the previous subsection, the outer capacitor has a capacitance C , while all inner capacitors have $2C$, as they mimic electrodes with electrolyte on

either sides. The charge on each of the capacitors is

$$Q_1(t) = 2C\Delta\Psi_1(t), \quad (\text{A8a})$$

...

$$Q_{n-1}(t) = 2C\Delta\Psi_{n-1}(t) \quad (\text{A8b})$$

$$Q_n(t) = C\Delta\Psi_n(t). \quad (\text{A8c})$$

Kirchoff's law states that

$$I = I_1 + I_{12}, \quad (\text{A9a})$$

$$I_{12} = I_2 + I_{23}, \quad (\text{A9b})$$

...

$$I_{(n-2)(n-1)} = I_{(n-1)} + I_{(n-1)n}, \quad (\text{A9c})$$

$$I_{(n-1)n} = I_n, \quad (\text{A9d})$$

which gives $I = I_1 + I_2 + \dots + I_n$. For the different currents, Ohm's law reads

$$IR = 2[\Psi - \Delta\Psi_1(t)], \quad (\text{A10a})$$

$$I_{12}R' = \Delta\Psi_1(t) - \Delta\Psi_2(t), \quad (\text{A10b})$$

$$I_{23}R' = \Delta\Psi_2(t) - \Delta\Psi_3(t), \quad (\text{A10c})$$

...

$$I_{(n-1)n}R' = \Delta\Psi_{(n-1)}(t) - \Delta\Psi_n(t). \quad (\text{A10d})$$

Combining the above equations gives n coupled differential equations

$$\Delta\dot{\Psi}_1(t) = \frac{I_1}{2C} = \frac{I - I_{12}}{2C} = \frac{\Psi}{RC} - \left(\frac{1}{RC} + \frac{1}{2R'C}\right)\Delta\Psi_1(t) + \frac{1}{2R'C}\Delta\Psi_2(t), \quad (\text{A11a})$$

$$\Delta\dot{\Psi}_2(t) = \frac{I_2}{2C} = \frac{I_{12} - I_{23}}{2C} = \frac{1}{2R'C}\Delta\Psi_1(t) - \frac{1}{R'C}\Delta\Psi_2(t) + \frac{1}{2R'C}\Delta\Psi_3(t), \quad (\text{A11b})$$

$$\begin{aligned} &\dots \\ \Delta\dot{\Psi}_n(t) &= \frac{I_n}{C} = \frac{1}{R'C}\Delta\Psi_{(n-1)}(t) - \frac{1}{R'C}\Delta\Psi_n(t), \end{aligned} \quad (\text{A11c})$$

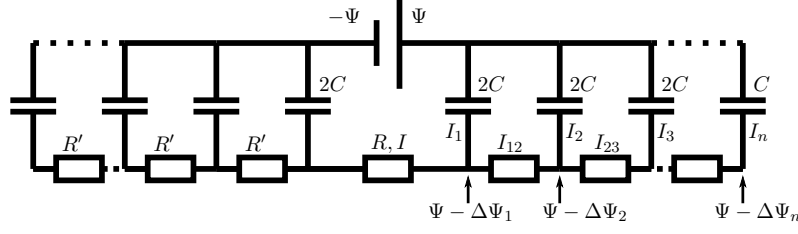


Figure A3. Equivalent circuit model for the stack electrode model for general n .

subject to n initial conditions: $\Delta\Psi_i(t=0) = 0$ for each $i = \{1, \dots, n\}$. In matrix form, Eq. (A11) reads

$$\begin{pmatrix} \dot{\Delta\Psi_1(t)} \\ \dot{\Delta\Psi_2(t)} \\ \dot{\Delta\Psi_3(t)} \\ \vdots \\ \dot{\Delta\Psi_n(t)} \end{pmatrix} = \frac{\Psi}{RC} \begin{pmatrix} 1 \\ 0 \\ \vdots \\ 0 \end{pmatrix} - \frac{1}{2R'C} \begin{pmatrix} 1 + \frac{H}{L(n-1)} & -1 & & & \\ -1 & 2 & -1 & & \\ & -1 & \ddots & \ddots & \\ & & \ddots & \ddots & -1 \\ & & & -1 & 2 & -1 \\ & & & & -2 & 2 \end{pmatrix} \begin{pmatrix} \Delta\Psi_1(t) \\ \Delta\Psi_2(t) \\ \Delta\Psi_3(t) \\ \vdots \\ \Delta\Psi_n(t) \end{pmatrix}, \quad (\text{A12})$$

which we again write as $\dot{X} = Y - MX$, where M is now a tridiagonal matrix that is Toeplitz except for two elements ($M_{1,1}$ and $M_{n,n-1}$). Note that, for the top left element we used $H = h(n-1)$ to rewrite $R'/R = h/(2L) = H/[2L(n-1)]$ hence $1 + 2R'/R = 1 + H/[L(n-1)]$. Again diagonalizing M as $M = UDU^{-1}$, the formal solution to Eq. (A12) reads

$$X(t) = U(1 - \exp[-Dt])D^{-1}U^{-1}Y, \quad (\text{A13})$$

with

$$1 - \exp[-Dt] = 1 - \begin{pmatrix} \exp\left[-\frac{t\lambda_1}{2R'C}\right] & & \\ & \ddots & \\ & & \exp\left[-\frac{t\lambda_n}{2R'C}\right] \end{pmatrix} \quad (\text{A14})$$

We used the above model to derive two key results of the main text. First, to obtain the data in Fig. 2(b) we diagonalized M numerically for the case $n = 5$. With the resulting equivalent circuit potential differences $\Delta\Psi_i(t)$ encoded in $X(t)$ [Eq. (A13)], we determine the surface charge densities $Ae\sigma_i(t) = C_i\Delta\Psi_i(t)$ on the electrodes of the stack electrode model. To do that, we use $C = A\epsilon\kappa$, $\Phi = e\Psi/k_B T$, and $X(t) = \Psi f(t)$, to write $\sigma_i(t) = [k_B T \epsilon / (e^2 \kappa^{-1})] \Phi f(t) = 2\rho_s \kappa^{-1} \Phi f(t)$. Results are shown in Fig. 2(b) with lines. In the same figure, we show numerical results of the PNP equation [Eqs. (1), (2), and (3)] with symbols. We see that, for $\Phi \ll 1$ and $\kappa L > \kappa h \gg 1$, the equivalent circuit model describes the behavior of the stack electrode model very well.

Second, to obtain Eq. (4), we proceed as follows. Writing $\lambda_- = \min\{\lambda_1, \dots, \lambda_n\}$, the longest relaxation time

reads $\tau_n = 2R'C/\lambda_- = \tau_{RC} \times 2H/[L(n-1)\lambda_-]$. We diagonalized M numerically for various n and H/L to find λ_- . The resulting τ_n , shown with symbols in Fig. A4(a), can be accurately approximated by $\tau_n = \tau_{RC}(f_1 + f_2 n)$: for the three H/L values considered, the residual of a least square fit was at most $R^2 = 0.00034$. In Fig. A4(b) we see that the coefficients f_1 and f_2 are roughly linear in H/L . We performed a second least-squares fit to determine the coefficients a_1, b_1, a_2 , and b_2 in $f_1 = a_1 + b_1 H/L$ and $f_2 = a_2 + b_2 H/L$. Note, however, that we can determine a_1 and b_1 analytically. In the limit $H/L \rightarrow 0$, i.e., $R'/R \rightarrow 0$, all capacitors in Fig. A3 are connected in parallel, yielding a total capacitance $C_{tot} = (2n-1)C$. Equation (A2) now applies, with C replaced by C_{tot} : we find $\tau_n = \tau_{RC}(2n-1)$. This means that we need to constrain $a_1 = -1$ and $a_2 = 2$ when fitting f_1 and f_2 . This

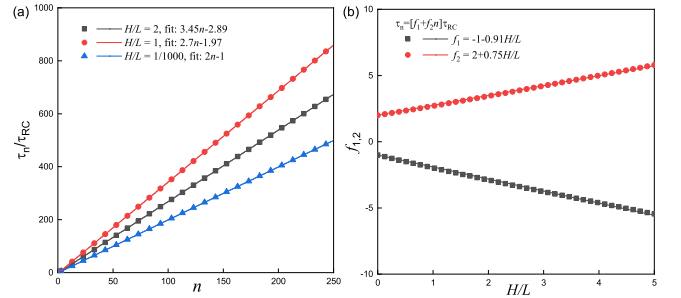


Figure A4. The slowest relaxation time τ_n of a n -electrode model as obtained with the smallest eigenvalue λ_- of the tridiagonal matrix M [cf. Eq. (A12)]. The lines in (a) indicate the least-squares fit $\tau_n/\tau_{RC} = f_1 + f_2 n$ through the data up to $n = 250$. In (b) we then find the fits $f_1 = -1 - 0.91H/L$, and $f_2 = 2 + 0.75H/L$.

ensures that, for $n = 1$ (for which $H/L = 0$), we correctly reproduce $\tau_n = \tau_{RC}$. Fitting to f_1 and f_2 -data at $n = 250$ [Fig. A4(a)], we find $b_1 = -0.91$ and $b_2 = 0.75$ [Fig. A4(b)]. Hence, the equivalent-circuit model predicts that all electrodes relax exponentially at late times with the same time constant

$$\frac{\tau_n}{\tau_{RC}} = \left[2 + 0.75 \frac{H}{L} \right] n - 1 - 0.91 \frac{H}{L}. \quad (\text{A15})$$

While the numerical factors in this equation were fitted to data up to $n = 250$, we have performed the same calculation up to $n = 90000$ and found that Eq. (A15) estimated the relaxation time within 1.3%. However, fits to f_1 and f_2 up to second order in H/L through the data up to $n = 250$ yield a corresponding $n = 90000$ relaxation time prediction accurate within 0.5%. Interestingly, we see that τ_n depends on salinity solely through τ_{RC} ; hence, τ_n decreases with increasing salt concentration.

Figure A5 is similar to Fig. 2(b), but we now show equivalent circuit predictions for $n = 250$ instead of $n = 5$. Shown also are the function $1 - \exp(-t/\tau_n)$ (blue) and the scaled total surface charge $\Sigma(t)/\Sigma_{eq}$ (red), with $\Sigma(t) = \sigma_1(t) + \sigma_2(t) + \dots + \sigma_n(t)$ and $\Sigma_{eq} = \Sigma(t/\tau_{RC} \rightarrow \infty)$. Even though $\Sigma(t)$ harbors n decaying exponential modes [related to all eigenvalues λ_i , see Eqs. (A13) and (A14)], we see that the total surface charge is approximated well by a single exponential decay with the longest relaxation time τ_n . In other words, the stack electrode model suggests that τ_n gives a good estimate for the relaxation of the charge on all n electrodes.

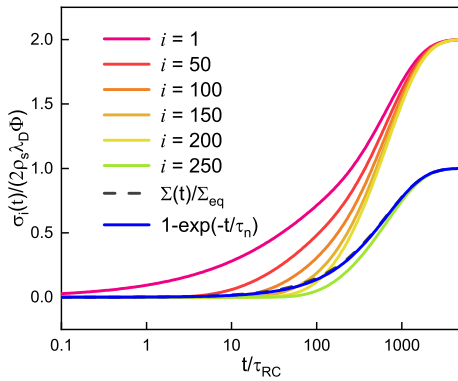


Figure A5. Time dependence of the scaled surface charge densities $\sigma_i(t)$ for $i = \{1, 50, 150, 200, 250\}$ for $H/L = 1$, and $n = 250$, as predicted by the equivalent circuit model. The colormap goes from red purple ($i = 1$) to light green ($i = n$). Shown also are the normalized total surface charge $\Sigma(t)/\Sigma_{eq}$ (dash black) and the function $1 - \exp(-t/\tau_n)$ (blue).

4. Relation to transmission line model

The circuit shown in Fig. A3 differs from the transmission line model in one place: the capacitance of the n -th electrode is C instead of $2C$. Tracing back the steps

of the derivation in the previous subsection, we find that for the transmission line model, Eqs. (A8c) and (A11c) obtain a factor 2 and $1/2$, respectively. This yields the same differential equation $\dot{X} = Y - MX$ where M is now given by

$$M = \frac{1}{2R'C} \begin{pmatrix} 1 + \frac{H}{L(n-1)} & -1 & & & \\ -1 & 2 & -1 & & \\ & -1 & \ddots & \ddots & \\ & & \ddots & \ddots & -1 \\ & & & -1 & 2 & -1 \\ & & & & -1 & 1 \end{pmatrix} \quad (\text{A16})$$

With the same methods as before, one could determine the late-time relaxation timescale, whose $H/L \rightarrow 0$ limit now reads $\tau_n = 2n\tau_{RC}$ because $C_{tot} = 2C$ in this case.

Appendix B: Additional numerical PNP data

In the main text we presented numerical results for the PNP equation (3) and its initial and boundary conditions [Eqs. (1) and (2)] for $H/L = 1$ and several Φ , n , κL . In this section we present additional data for other parameters to reinforce some of the main conclusions of our analysis.

First, we discussed the case $\Phi = 0.001$, $\kappa L = 100$, $H/L = 1$, and $n = 5$. For the same parameters except $n = \{3, 6, 11\}$, in Fig. B1 we present PNP data for the outer-electrode unit surface charge density $\sigma_n(t)$. Here, time is scaled either by τ_{RC} [Fig. B1(a)] or by τ_n [Fig. B1(b)]. The data collapse that we observe in the latter case again shows the value of the equivalent circuit model in describing the small- Φ relaxation of our setup.

Second, in Fig. 3 we studied the influence of Φ and n on our setup through two parameter sets: $\Phi = \{0.01, 0.1, 1, 2\}$, $\kappa L = 100$, $H/L = 1$, and $n = 1$; and $\Phi = 2$, $\kappa L = 100$, $H/L = 1$, and $n = \{2, 3, 6\}$. We now

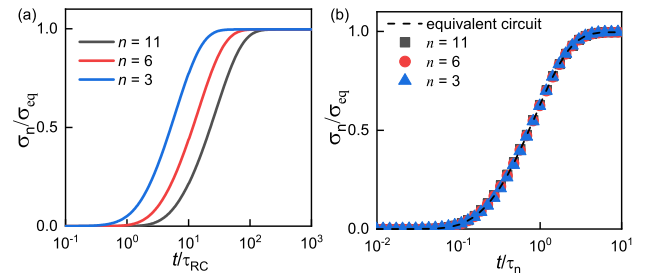


Figure B1. The surface charge density $\sigma_n(t)$ of the outer electrode from the numerical calculation of Eqs. (1)–(3) for $\Phi = 0.001$, $\kappa L = 100$, $H/L = 1$ and different n . We scale time by either by τ_{RC} (a) or by τ_n (b). The dashed line is the function $\sigma(t)/\sigma_{eq} = 1 - \exp[-t/\tau_n]$.

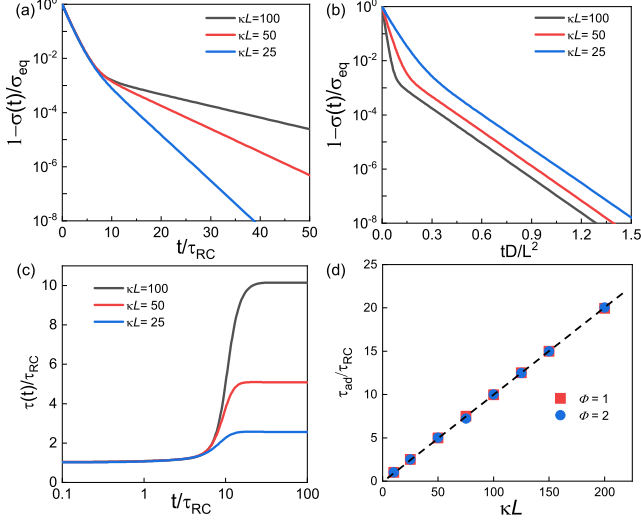


Figure B2. (a), (b), and (c) Charging dynamics of the stack-electrode model at $\Phi = 1$, $\kappa L = \{25, 50, 100\}$, $H/L = 0$ and $n = 1$. We show $1 - \sigma(t)/\sigma_{eq}$ with time scaled either by τ_{RC} (a) or by L^2/D (b). (c) The timescale $\tau(t)$ [Eq. (B1)]. (d) The equilibrium relaxation timescale τ_{ad} as function of κL for $\Phi = 1$ and 2 , $n = 1$ and $H/L = 0$.

use $\Phi = 2$, $\kappa L = \{25, 50, 100\}$, $H/L = 0$, and $n = 1$ to study the influence of κL . We show $1 - \sigma(t)/\sigma_{eq}$ with time scaled either by τ_{RC} [Fig. B2(a)] or by L^2/D [Fig. B2(b)]. In the first case, $1 - \sigma(t)/\sigma_{eq}$ collapses at early times for the different κL . This reinforces our finding of Fig. 3(e) where we found a similar early-time collapse for different Φ , from which we concluded that the early-time relaxation of $1 - \sigma(t)/\sigma_{eq}$ is described well by the equivalent circuit model. In the same figure [Fig. 3(e)] we saw that $1 - \sigma(t)/\sigma_{eq}$ relaxes on two timescales. We further investigate the second, slower timescale in Fig. B2(b), where time is scaled by L^2/D . We see there that $1 - \sigma(t)/\sigma_{eq}$ relaxes at late times with the same timescale for the different κL . To characterize both the early- and late-time response, we define a time-dependent function $\tau(t)$,

$$\tau(t) = - \left[\frac{d \ln(1 - \sigma(t)/\sigma_{eq})}{dt} \right]^{-1} \quad (\text{B1})$$

that, for a purely exponential charge buildup $\sigma(t) = \sigma_{eq}[1 - \exp(-t/\tau^*)]$ yields $\tau(t) = \tau^*$. Figure B2(c) presents $\tau(t)$ for the same parameters as used in Fig. B1(a) and (b). At early times ($t/\tau_{RC} < 1$), $\tau(t) = \tau_{RC}$, while at late times ($t/\tau_{RC} > 1$), $\tau(t)$ shoots up to different plateaus τ_{ad} for different κL . In Fig. B2(d) we plot τ_{ad} against κL for $\Phi = 1$ and $\Phi = 2$ and find a linear relation $\tau_{ad}/\tau_{RC} = 0.1\kappa L$, hence $\tau_{ad} = 0.1L^2/D$ (if $n = 1$).

Third, as mentioned above, we discussed the case $\Phi = 2$, $\kappa L = 100$, $H/L = 1$, and $n = \{2, 3, 6\}$. Here, we present additional data for the same Φ , κL , and H/L for $n = \{2, 3, 6, 11, 21\}$. Notably, these values correspond to $\kappa h = \{100, 50, 20, 10, 5\}$, which means that we

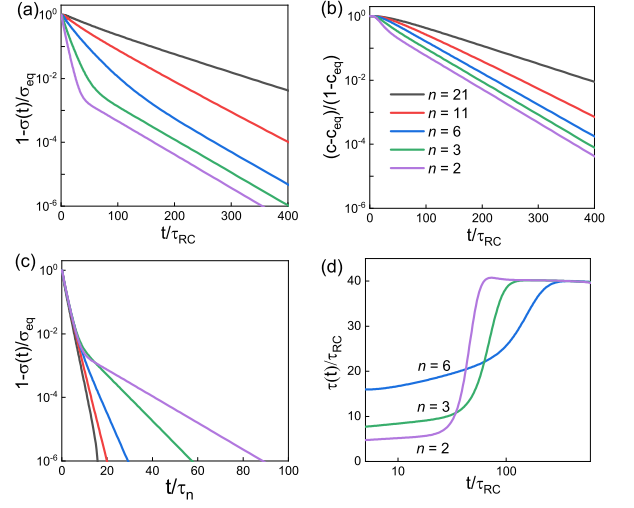


Figure B3. (a), (b), and (c) Charging dynamics of the stack-electrode model at $\Phi = 2$, $\kappa L = 100$, $H/L = 1$, and $n = \{2, 3, 6, 11, 21\}$. (a) The charging relaxation $1 - \sigma(t)/\sigma_{eq}$ and (b) the concentration decay $(c(t) - c_{eq})/(c(0) - c_{eq})$. In (c) we plot the same data as in (a), but with time scaled by τ_n instead of by τ_{RC} . (d) The $\tau(t)$ [Eq. (B1)] for $n = \{2, 3, 6\}$ and Φ , κL , and H/L as in (a), (b), and (c).

probe the behavior of the stack-electrode model for both non-overlapping and overlapping EDLs. As noted in the main text, Fig. B3(a) again shows that increased porosity (higher n) leads to slower surface charge buildup. Moreover, we see that $1 - \sigma(t)/\sigma_{eq}$ relaxes at late times with the same timescale for the $n = \{2, 3, 6\}$, while for $n = 11$ and $n = 21$ (corresponding to $\kappa h = 10$ and $\kappa h = 5$) it relaxes slower, arguably because EDLs overlap. The same conclusions hold for $(c(t) - c_{eq})/(c(0) - c_{eq})$, which we plot in Fig. B3(b). In Fig. B3(c) we plot the same data as in Fig. B3(a), but with time scaled by τ_n instead of by τ_{RC} . We see there that $1 - \sigma(t)/\sigma_{eq}$ collapses at early times for all n considered, which again confirms the early-time τ_n scaling. For completeness, in Fig. B3(d), we again evaluated $\tau(t)$ as defined in Eq. (B1): similar to the $n = 1$ case, two plateaus appear.

Appendix C: Dynamic density functional theory for concentrated electrolytes

In the main text, we discussed the charging dynamics of the electrodes by both the equivalent circuit model and the classical Poisson-Nernst-Planck, which both are meaningful for low charging potentials and dilute electrolytes. We now examine higher applied potentials and high concentrations by classical dynamic density functional theory (DDFT), where both the equivalent circuit model and the Poisson-Nernst-Planck equations are expected to fail. For ion diffusion between two charged electrodes, DDFT asserts that the time evolution for the

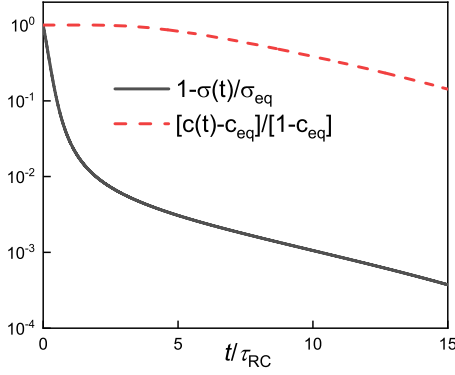


Figure C1. The charge relaxation $1 - \sigma(t)/\sigma_{eq}$ (solid line) and the concentration decay $(c(t) - c_{eq})/(1 - c_{eq})$ (dashed line) for a 1 M ionic liquid electrolyte at $\Phi = 20$, $L/a = 12$, $H/L = 0$, $\kappa^{-1} = 4.86 \times 10^{-11}$ nm, and $n = 1$.

local density profiles of ionic species [21, 23], again follows Eq. (3) with $j_{\pm}(x, t)$ replaced by

$$j_{\pm}(x, t) = -\frac{D}{k_B T} \rho_{\pm}(x, t) \partial_x \left(\frac{\delta F[\rho_+, \rho_-]}{\delta \rho_{\pm}(x, t)} \right), \quad (C1)$$

with $F[\rho_+, \rho_-]$ being the free energy functional, for which a suitable approximation needs to be made. To model electrolyte solutions, $F[\rho_+, \rho_-]$ should contain at least an ideal-solution term and the mean electrostatic potential. Moreover, we model contributions from ionic excluded volume effects through the functional described in Ref. [21, 23]. The restricted primitive model is used to represent a room-temperature ionic liquid wherein both cations and anions are approximated by monovalent charged hard spheres. The diameters of cation and anion are both $a = 0.5$ nm (corresponding to the averaged size of EMI and TFSI), the concentration is $\rho_b = 1$ M, the diffusion coefficient for the ionic liquid are $D = 4.3 \times 10^{-11}$ m² s⁻¹, and the dielectric constant is set as $\epsilon = 2$.

Fig. C1 shows DDFT result for the evolving surface charge density $1 - \sigma(t)/\sigma_{eq}$ (solid lines) and the normalized salt concentration at the cell center $(c(t) - c_{eq})/(1 - c_{eq})$ (dashed lines). We observe interesting similarities to the PNP data presented in Fig. 3(e): the surface charge density exhibits two distinct relaxation times and, at late times, $1 - \sigma(t)/\sigma_{eq}$ and $(c(t) - c_{eq})/(1 - c_{eq})$ decay with the same time constant. Qualitatively, this is very similar to our PNP results, and illustrate the robustness of our PNP findings regarding the existence of two timescales that govern coupled charge and salt transport. However, a direct comparison between our DDFT and PNP results is difficult for the following reasons: First, PNP reduces to Poisson-Boltzmann theory at equilibrium. Boltzmann weights $\exp(\Phi)$ would predict unphysically large counterion densities close to the electrode surfaces. Second, the RTIL has a tiny Debye length. Recent experimental studies, however, have suggested that, instead of κ^{-1} , an anomalously large electrostatic screening length λ_S gov-

erns the electrostatic interactions of dense electrolytes and RTILs [44]. It would be interesting to find whether λ_S replaces λ_D in the RC time of the $n = 1$ circuit. However, as dense electrolytes and RTILs, even at equilibrium, are currently a hotly debated topic, a full characterization of the out-of-equilibrium behavior of our $n > 1$ stack electrode model is beyond the scope of the current article. A more detailed and quantitative comparison of the PNP and DDFT results will be presented elsewhere.

Appendix D: Comparison to experimental surface charge build up

In the main text, we determined τ_n and τ_{ad} for parameters corresponding to the experimental setup of Ref. [26]. Here, We reanalyze data of that paper for the decaying electric current $I(t)$ caused by an applied potential $\Psi = 0.3$. Repeated measurements were performed at different ρ_b : twice at $\rho_b = \{0.001, 0.01, 0.1\}$ M and four times at $\rho_b = 1$ M. Figure D1(a) shows the average currents $I(t)$ of those measurements for each ρ_b . Dotted and dash-dotted lines in Fig. D1(a) show two exponential decays with time constants $\tau_1 = 200$ s and $\tau_2 = 9000$ s. With these lines one sees for $\rho_b = 1$ M that $I(t)$ decays exponentially at late times, while at early times its behavior is more complicated. Figure D1(b) shows $Q(t) = \int_0^t I(t)$, determined numerically by integrating an interpolation through the data of Fig. D1(a). Also shown with a dashed line is the function $Q(t) = \{1.8[1 - \exp(-t/\tau_1)] + 0.1[1 - \exp(-t/\tau_2)]\} C$, where the numerical prefactors were fixed by eye. This dashed line describes $Q(t)$ properly after $t \approx 3000$ s, underestimating $Q(t)$ at earlier times. We saw in Fig. A5 that the stack electrode model displays a similar feature: at intermediate times, the total surface charge $\Sigma(t)$ is larger than $1 - \exp(-t/\tau_n)$. The difference between these two observables, however, is much smaller in the stack elec-

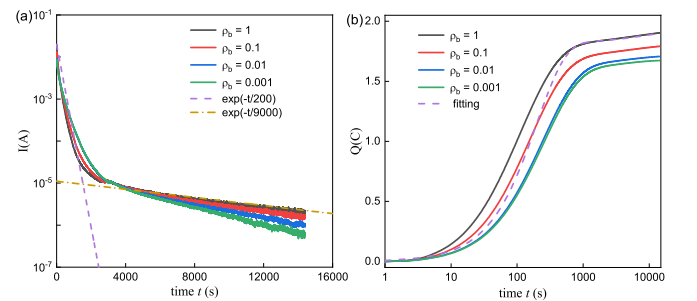


Figure D1. (a) Experimental data of Ref. [26] (dots) for the current relaxation of porous electrodes subject to a suddenly imposed potential $\Psi = 0.3$ V. (b) The total surface charge Q , found by integrating the data from (a). The dash line is a fit by eye: $Q = \{1.8[1 - \exp(-t/200)] + 0.1[1 - \exp(-t/9000)]\} C$, whose two time constants were inspired by the dotted and dash-dotted lines in (a).

trode model than in the experiments. Hence, our stack electrode model does not yet fully explain the experimental data of Ref. [26]. Still, comparing the fitted time constants $\tau_1 = 200$ s and $\tau_2 = 9000$ s to $\tau_n = 2.9 \times 10^2$ s and $\tau_{ad} = 4.8 \times 10^2$ s as stated in the main text, respectively, we see that our model predicts both timescales within

approximately one order of magnitude. Even though we seem to predict τ_1 better than τ_2 , using a smaller diffusion constant $D = 2 \times 10^{-10}$ m² s⁻¹, to account for slow diffusion in pores [32, 41], leads to $\tau_n = 2.3 \times 10^3$ s and $\tau_{ad} = 3.6 \times 10^3$ s and predictions for τ_2 are better than for τ_1 .

-
- [1] J. Chmiola, G. Yushin, Y. Gogotsi, C. Portet, P. Simon, and P.-L. Taberna, *Science* **313**, 1760 (2006).
 - [2] D. T. Limmer, C. Merlet, M. Salanne, D. Chandler, P. A. Madden, R. van Roij, and B. Rotenberg, *Phys. Rev. Lett.* **111**, 106102 (2013).
 - [3] A. C. Forse, J. M. Griffin, C. Merlet, J. Carretero-Gonzalez, A.-R. O. Raji, N. M. Trease, and C. P. Grey, *Nat. Energy* **2**, 16216 (2017).
 - [4] C. Prehal, C. Koczwara, H. Amenitsch, V. Presser, and O. Paris, *Nat. Commun.* **9**, 4145 (2018).
 - [5] P. Simon and Y. Gogotsi, *Acc. Chem. Res.* **46**, 1094 (2013).
 - [6] C. Cheng, G. Jiang, C. J. Garvey, Y. Wang, G. P. Simon, J. Z. Liu, and D. Li, *Sci. Adv.* **2**, e1501272 (2016).
 - [7] T. Mouterde, A. Keerthi, A. R. Poggioli, S. A. Dar, A. Siria, A. K. Geim, L. Bocquet, and B. Radha, *Nature* **567**, 87 (2019).
 - [8] R. de Levie, *Electrochim. Acta* **8**, 751 (1963).
 - [9] M. Mirzadeh, F. Gibou, and T. M. Squires, *Phys. Rev. Lett.* **113**, 097701 (2014).
 - [10] R. Tivony, S. Safran, P. Pincus, G. Silbert, and J. Klein, *Nat. Commun.* **9**, 4203 (2018).
 - [11] L. Helseth, *J. Energy Storage* **25**, 100912 (2019).
 - [12] G. Feng and P. T. Cummings, *J. Phys. Chem. Lett.* **2**, 2859 (2011).
 - [13] S. Kondrat, P. Wu, R. Qiao, and A. A. Kornyshev, *Nat. Mater.* **13**, 387 (2014).
 - [14] C. Péan, C. Merlet, B. Rotenberg, P. A. Madden, P.-L. Taberna, B. Daffos, M. Salanne, and P. Simon, *ACS Nano* **8**, 1576 (2014).
 - [15] K. Breitsprecher, C. Holm, and S. Kondrat, *ACS Nano* **12**, 9733 (2018).
 - [16] G. Feng, M. Chen, S. Bi, Z. A. H. Goodwin, E. B. Postnikov, N. Brilliantov, M. Urbakh, and A. A. Kornyshev, *Phys. Rev. X* **9**, 021024 (2019).
 - [17] C. Noh and Y. Jung, *Phys. Chem. Chem. Phys.* **21**, 6790 (2019).
 - [18] S. Bi, M. Chen, R. Wang, J. Feng, M. Dinca, A. A. Kornyshev, and G. Feng, *Nat. Mater.* (2020).
 - [19] A. Chatterji and J. Horbach, *J. Chem. Phys.* **126**, 064907 (2007).
 - [20] A. J. Asta, I. Palaia, E. Trizac, M. Levesque, and B. Rotenberg, *J. Chem. Phys.* **151**, 114104 (2019).
 - [21] C. Lian, S. Zhao, H. Liu, and J. Wu, *J. Chem. Phys.* **145**, 204707 (2016).
 - [22] S. Babel, M. Eikerling, and H. Löwen, *J. Phys. Chem. C* **122**, 21724 (2018).
 - [23] J. Jiang, D. Cao, D.-e. Jiang, and J. Wu, *J. Phys. Chem. Lett.* **5**, 2195 (2014).
 - [24] D. Brogioli, R. Zhao, and P. M. Biesheuvel, *Energy Environ. Sci.* **4**, 772 (2011).
 - [25] C. Lian, K. Liu, K. L. van Aken, Y. Gogotsi, D. J. Wesolowski, H. L. Liu, D. E. Jiang, and J. Z. Wu, *ACS Energy Lett.* **1**, 21 (2016).
 - [26] M. Janssen, E. Griffioen, P. M. Biesheuvel, R. van Roij, and B. H. Ern , *Phys. Rev. Lett.* **119**, 166002 (2017).
 - [27] A. S. Ambrozevich, S. A. Ambrozevich, R. T. Sibatov, and V. V. Uchaikin, *Russ. Electr. Eng.* **89**, 64 (2018).
 - [28] M. Z. Bazant, K. Thornton, and A. Ajdari, *Phys. Rev. E* **70**, 021506 (2004).
 - [29] M. Janssen and M. Bier, *Phys. Rev. E* **97**, 052616 (2018).
 - [30] I. Palaia, PhD thesis, Universit  Paris-Saclay 2019, (private communication).
 - [31] M. Janssen, *Phys. Rev. E* **100**, 042602 (2019).
 - [32] H. Sakaguchi and R. Baba, *Phys. Rev. E* **76**, 011501 (2007).
 - [33] P. M. Biesheuvel and M. Z. Bazant, *Phys. Rev. E* **81**, 031502 (2010).
 - [34] R. Zhao, O. Satpradit, H. H. M. Rijnaarts, P. M. Biesheuvel, and A. van der Wal, *Water Res.* **47**, 1941 (2013).
 - [35] A. Obliger, M. Jardat, D. Coelho, S. Bekri, and B. Rotenberg, *Phys. Rev. E* **89**, 043013 (2014).
 - [36] L. Pilon, H. Wang, and A. L. d'Entremont, *J. Electrochem. Soc.* **162**, A5158 (2015).
 - [37] C. Lian, H. Su, C. Li, H. Liu, and J. Wu, *ACS Nano* **13**, 8185 (2019).
 - [38] A. Eftekhari, *ACS Sustain. Chem. Eng.* **7**, 3692 (2019).
 - [39] L. H jgaard Olesen, M. Z. Bazant, and H. Bruus, *Phys. Rev. E* **82**, 011501 (2010).
 - [40] N. Boon and R. van Roij, *Mol. Phys.* **109**, 1229 (2011).
 - [41] E. Allahyarov, H. Lwen, and P. L. Taylor, *Electrochim. Acta* **242**, 73 (2017).
 - [42] M. Janssen and M. Bier, *Phys. Rev. E* **99**, 042136 (2019).
 - [43] P. A. J. Kouyzer, Master's thesis, Utrecht University 2015.
 - [44] M. A. Gebbie, A. M. Smith, H. A. Dobbs, A. A. Lee, G. G. Warr, X. Banquy, M. Valtiner, M. W. Rutland, J. N. Israelachvili, S. Perkin, and R. Atkin, *Chem. Commun.* **53**, 1214 (2017).